

ORIGINAL RESEARCH ARTICLE

Influence of powder morphology on laser absorption behavior and printability of nanoparticle-coated 90W-Ni-Fe powder during laser powder bed fusion

Jingjia Sun, Meng Guo, Keyu Shi, Dongdong Gu*

Jiangsu Provincial Engineering Laboratory for Laser Additive Manufacturing of High-Performance Metallic Components, College of Materials Science and Technology, Nanjing University of Aeronautics and Astronautics, Nanjing, China

Abstract

In this work, mesoscopic simulation and experimental studies were applied to investigate the influence of powder morphology and characteristics on laser absorption behavior and printability of nanoparticle-coated 90W-Ni-Fe powder during laser powder bed fusion (LPBF). The mechanism of laser-material interaction and the thermal behavior of molten fluid during LPBF were revealed, thereby optimizing the powder preparation parameters. It showed that when the powder preparation parameters were optimized (i.e., ball-to-powder weight ratio of 1:2, milling speed of 250 rpm, and milling time of 6 h), the Ni and Fe nanoparticles were uniformly dispersed on W particles and, meanwhile, the sufficiently high sphericity of the W matrix particles was maintained. The nanoparticle-coated 90W-Ni-Fe powder had a sound laser absorption behavior with laser absorptivity of 93.51%, leading to the high LPBF printing quality with a smooth surface free of balling phenomenon and microcracks. Specimen fabricated using optimally prepared powder has a high density of 98% and a low surface roughness of 7.91 μm . The LPBF-processed 90W-Ni-Fe alloys had a uniform hardness distribution with an average value of 439.47 HV_1 and significantly enhanced compression properties with compressive strength of 1255.35 MPa and an elongation of 24.74%. The results in this work provided a physical understanding of complex and interdependent laser-powder interaction and melt pool formation mechanisms during LPBF of W-based alloys that are governed by powder characteristics.

***Corresponding author:**
Dongdong Gu
(dongdonggu@nuaa.edu.cn)

Citation: Sun J, Guo M, Shi K, *et al.*, 2022, Influence of powder morphology on laser absorption behavior and printability of nanoparticle-coated 90W-Ni-Fe powder during laser powder bed fusion. *Mater Sci Add Manuf.* 1(2): 11. <http://doi.org/10.18063/msam.v1i2.11>

Received: April 11, 2022

Accepted: May 30, 2022

Published Online: June 14, 2022

Copyright: © 2022 Author(s). This is an Open Access article distributed under the terms of the Creative Commons Attribution License, permitting distribution, and reproduction in any medium, provided the original work is properly cited.

Publisher's Note: Whioce Publishing remains neutral with regard to jurisdictional claims in published maps and institutional affiliations.

Keywords: Laser powder bed fusion; Powder morphology; Laser absorption behavior; Mechanical properties

1. Introduction

W-Ni-Fe has attracted a great deal of attention in the fields of national defense, industry, and military due to its high density, high melting point, and extremely low thermal expansion coefficient^[1,2]. However, at present, they are usually fabricated by conventional powder metallurgy technique based on liquid phase sintering, which is characterized by costly mold cycles and difficulty in completely melting W particles, limiting the application of

W-Ni-Fe as a structural material. The rapid development of additive manufacturing (AM) provides a new method for W-Ni-Fe fabrication. AM is defined as a method of printing components from three-dimensional (3D) model data using a layer-wise manufacturing philosophy and can be divided into seven divisions according to printing mechanism and raw material^[3]. Laser powder bed fusion (LPBF) is one of the most promising AM technologies due to its laser-induced complete melting mechanism^[4,5]. As an efficient, digital, and highly flexible advanced technology, LPBF has been applied in many fields such as military, aerospace, and biomedical, and has a laser beam with high energy to completely melt W particles, making it one of the effective methods to prepare high-performance W-Ni-Fe components^[3,6]. Nevertheless, the design of raw materials has become a constraint to the development of LPBF-fabricated W-Ni-Fe parts^[3,5,6].

The previous studies indicate that powder properties have an important influence on LPBF-processed W parts. Field *et al.*^[7] produced W specimens with two kinds of high-purity W powders: the first powder was a chemically reduced powder with an irregular morphology, and the second powder was a plasma-spheroidized powder with highly spherical morphology. They found that W powders with high sphericity had higher apparent power densities and enhanced the density of LPBF-fabricated W components. A 3D laser absorption model based on ray tracing was established by Zhang *et al.*^[8] to investigate the influence of W particle size and its distribution on the powder-to-laser absorptivity and underlying behavior. The simulation and experimental results indicated that the absorptivity of the powder layers considerably exceeded the single powder particle value or the dense solid material value, and smaller particle size improved the laser absorptivity during LPBF-processed W parts. Braun *et al.*^[9] analyzed the processing of Mo and W by LPBF, and they identified the oxygen in the powder as a cause for cracks and residual porosity. Nevertheless, these studies mainly focused on pure W, and the effect of feedstock powder characteristics on laser absorption behavior and printing quality of LPBF-processed W-based alloys was rarely studied. It has been reported that nano-reinforcing particles can effectively improve the printing quality of LPBF-fabricated W-based alloys^[7,10-12].

Several studies have been carried out on laser absorption and melting behavior during LPBF. Khairallah *et al.*^[13] used high-fidelity simulations, coupled with synchrotron experiments, to capture fast multitransient dynamics at the meso-nanosecond scale. They discovered new spatter-induced defect formation mechanisms, which depend on the scan strategy and competition between

laser shadowing and expulsion. A recent study by Ge *et al.*^[14] proposed mesoscopic simulation to investigate the influence of ceramic addition on the laser energy absorption and powder melting behaviors during LPBF of TiC/Ti6Al4V composites, and they found that the addition of 1 wt.% or 3 wt.% ceramic was beneficial to improving the laser absorptivity and the surface morphology of melted track. A high-fidelity model coupled with a ray-tracing method was constructed by Ren *et al.*^[15] to visualize the flow kinetics and reflection behavior during LPBF of Cu-Cr-Zr alloy, which showed good agreement with experiments in terms of track width and depth. The above-mentioned and related studies have reported that laser absorptivity is vital for the subsequent metallurgical behavior and printing quality, and the absorption behavior and liquid-solid interface dynamics during LPBF are affected by the morphology and characteristics of feedstock powder. Understanding the complex and interdependent laser-powder-melt pool interaction during LPBF is of great importance, which matters for the control of metallurgical defects and mechanical properties of LPBF-fabricated W-based parts^[8,13,14,16]. However, few studies on laser absorption and melting behavior of W-based powders during LPBF have been reported, and the mechanisms of the influence of powder morphology and characteristics on laser absorption behavior and printability of 90W-Ni-Fe powder during LPBF remain unknown.

The *in situ* alloying of AM, as opposed to pre-alloyed powder used for printing, provides a feasible way for AM with multiple materials. The LPBF, due to its concentrated laser energy input with sufficiently high thermal behavior, is expected to become one of the *in situ* alloying processes in the coming years^[17-20]. In this work, the geometrical optical ray-tracing (GO-RT) models and computational fluid dynamics-based powder melting (CFD-PM) models were established to obtain an in-depth understanding of mechanisms during LPBF fabrication of W-based alloys. The nanoparticle-coated 90W-Ni-Fe powders for LPBF were fabricated by mechanical mixing with ball milling, and the corresponding LPBF experiments were carried out. The influence of the powder morphology and characteristics on laser absorption behavior and printability of LPBF 90W-Ni-Fe was investigated by numerical and experimental methods, and the laser-powder interaction mechanism and thermal behavior of molten fluid were revealed. A good agreement was obtained between the simulated and experimental results, and this work provided a physical understanding of complex and interdependent laser-powder-melt pool interaction during LPBF of 90W-Ni-Fe, aiming to form scientific guidance for LPBF fabricating high-quality W-based alloys.

2. Materials and methods

2.1. Powder preparation and LPBF printing

This work utilized the commercial spherical W powder and nano-scale Ni and Fe powder as starting materials (Figure 1), and an E2000 vertical inverter ball mill was used to prepare nanoparticle-coated 90W-Ni-Fe powders with different morphologies. The W powder had a size distribution of $D_{10} = 8.25 \mu\text{m}$, $D_{50} = 14.41 \mu\text{m}$, and $D_{90} = 24.25 \mu\text{m}$, respectively. The laser absorptivity/reflection of different powders was tested using a Shimadzu UV3600 UV-Vis NIR spectrophotometer, and the morphology of different powders was observed using a Hitachi S-4800 field emission scanning electron microscope (SEM).

The LPBF printing device was developed by the Nanjing University of Aeronautics and Astronautics, and the process details were described in our previous work^[21]. High-purity argon (99.9%) was used as the protective gas to prevent the formation of oxides, and a chessboard scanning strategy was employed to reduce heat accumulation during LPBF printing^[9]. The LPBF processing parameters of 90W-Ni-Fe alloys were laser power of 200 W, scanning speed of 250 mm/s, hatch spacing of 50 μm , and layer thickness of 30 μm . The length of the LPBF-fabricated single tracks was 50 mm, the size of block specimens was 6 mm \times 8 mm \times 8 mm, and the length to diameter (L/D) of the compression parts was 1.25 (GB/T 7314-2017).

2.2. Microstructure and mechanical properties

The top surface morphologies of 90W-Ni-Fe scanning tracks and block specimens were observed using SEM, and the block specimens were ground and polished according to the standard metallographic procedures and were observed using an XJP-300 optical microscope (OM). The 3D morphology and the surface roughness of 90W-Ni-Fe alloys were obtained using a VK-150K 3D laser microscope imaging system. The microhardness of the optimal 90W-Ni-Fe sample was tested using an HXS-1000 AY microhardness tester with a load setting of 1000 g, and the stress distribution was obtained by a Proto LXR high-speed X-ray residual stress analyzer. The compression

experiment was carried out using a CMT5205 testing machine with a loading rate of 1 mm/min.

2.3. Establishment of GO-RT models

Numerical simulations in this work were based on the mechanism of LPBF (Figure 2A), and a random function was used to generate powder beds in MATLAB (Figure 2B). The geometric information was imported into the optical design and analysis software FRED to form geometric models. After establishing the geometric models, according to Fresnel formulae, the laser reflection behavior was described as^[16,22]:

$$\alpha_p = 1 - \frac{(n_c - 1 / \cos\theta) + m_c^2}{(n_c + 1 / \cos\theta) + m_c^2} \quad (1)$$

$$\alpha_s = 1 - \frac{(n_c - \cos\theta) + m_c^2}{(n_c + \cos\theta) + m_c^2} \quad (2)$$

where α denotes the absorptivity, θ is the angle of incidence, n_c represents the real part of the complex index of refraction, and m_c represents the imaginary part of the complex index of refraction^[14,22]. In this study, the laser refractive behavior of different materials was described by defining the complex index of refraction (Figure 3). Integrating sphere is one of the laser absorption/reflectivity measurement methods (Figure 4A). By the laser absorbance formula:

$$A = 1 - T - R \quad (3)$$

where A denotes the absorption, T is the transmission, and R represents the radiation reflection. The transmitted radiation of metal can be generally regarded as zero^[8]. Therefore, the above equation can be simplified as:

$$A = 1 - R \quad (4)$$

this means the absorption of the laser energy can be calculated using the measured reflectivity^[14,22]. After obtaining a powder bed with indices defined, a spherical analytical surface was established according to the principle of integrating sphere. At the same time, a Gaussian distributed optical source similar to the LPBF equipment was loaded above the powder bed (Figure 4B). Subsequently, ray tracing was performed in FRED to investigate the laser absorption behavior (Figure 4C and D).

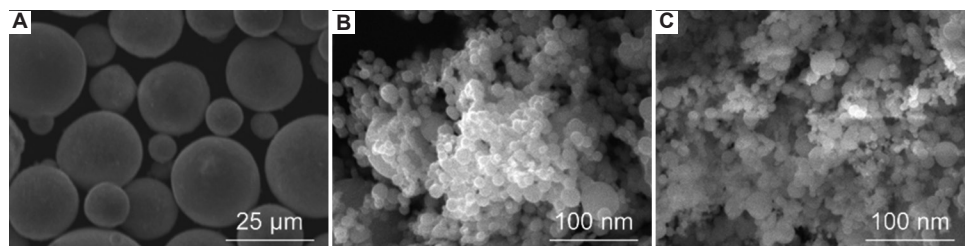


Figure 1. SEM images showing the starting powders: W (A), Ni (B), and Fe (C).

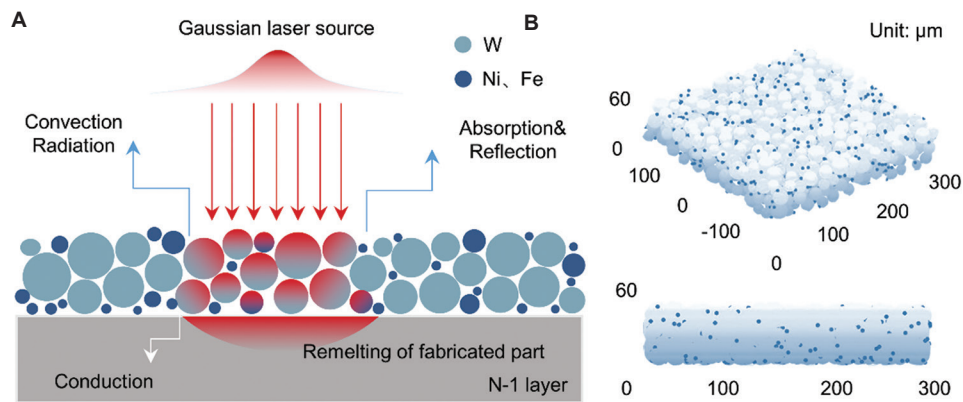


Figure 2. Mechanism of LPBF processing (A) and the algorithmically generated powder bed (B).

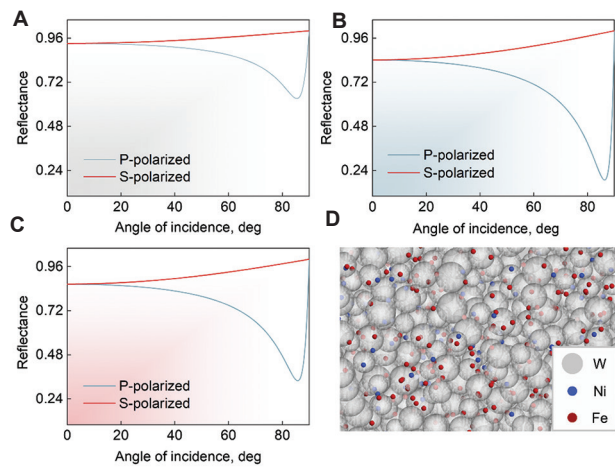


Figure 3. Fresnel formulae for calculating absorptivity for S and P polarization of W (A), Ni (B), and Fe (C), and the powder bed with indices defined (D).

2.4. Establishment of CFD-PM models

Geometric information was also imported into the computational fluid dynamics simulation software FLUENT. During the construction of the CFD-PM model, the laser energy conversion factor of the volumetric Gaussian heat source was set concerning simulation and experimental results. The modified heat flow distribution of the moving Gaussian heat source can be described as^[14,23,24]:

$$q = \frac{6PA}{R^2\pi H(1-1/e^3)} \exp\left(\frac{-9(x^2 + y^2)}{R^2 \log(H/z)}\right) \quad (5)$$

where P is the laser power, R is the spot radius, and is the laser heat source depth. Considering that most of the heat was conducted by the powder bed and solidification layer, the boundary conditions were described as^[24]:

$$K \frac{\partial T}{\partial n} + h_c(T - T_0) + \sigma\varepsilon(T^4 - T_0^4) = q \quad (6)$$

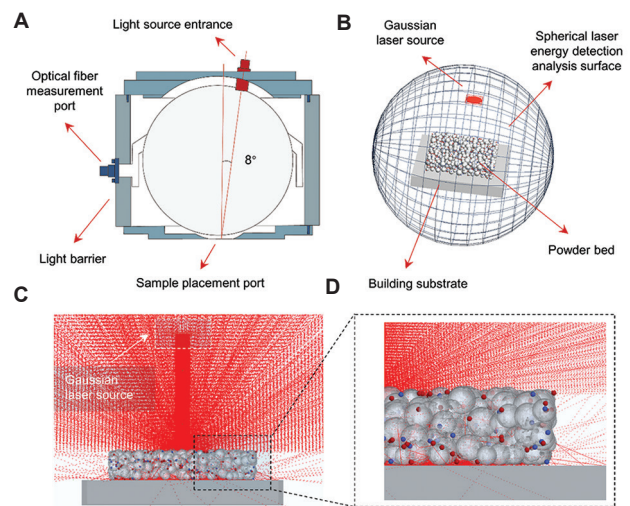


Figure 4. Schematic diagram of integrating sphere (A), GO-RT model with Gaussian laser source and spherical analytical surface (B), and complicated interaction between the powder bed and laser beam (C and D).

where T_0 is the surrounding temperature, h_c is the heat conduction coefficient, σ is the Stefan-Boltzmann constant, and ε is the emissivity. The side and bottom boundaries were settled as insulation boundaries^[14]. More modeling details were set concerning existing reports to illustrate the effect of nanoparticle-coated 90W-Ni-Fe powder morphology on the non-uniform melting behavior during LPBF^[8,13,14,22-25].

3. Results and discussion

3.1. Effects of nanoparticle-coated 90W-Ni-Fe powder morphologies on the laser absorption behavior

Before establishing models, the morphologies of nanoparticle-coated 90W-Ni-Fe powder were observed. Energy input during the milling process was different under different milling conditions, thus producing nanoparticle-coated 90W-Ni-Fe powder with different

morphologies^[10,11,25-27]. According to the specific impact energy equation^[28]:

$$E_i = \sum_{j=1}^n \frac{1}{2M_s} M_b v_j^2 \quad (7)$$

where, E_i is the specific impact energy in ball milling, M_s is the mass of powder, M_b is the total mass of grinding balls, v_j is the relative impact velocity between two grinding balls and/or a ball grinding against the grinding bowl wall, and n is the number of collision of a ball against other balls and/or the grinding bowl wall within a second. As can be seen from the above equation, the higher the milling speed or ball-to-powder weight ratio is applied, the higher the impact energy is obtained. The nanoparticle-coated 90W-Ni-Fe powder morphology evolved with the change of milling energy (Figure 5A). Reinforced particles were gradually dispersed uniformly with increased specific impact energy in ball milling, but particle deformation and breakage were more likely to occur (Figure 5B). When the ball-to-powder weight ratio was 1:2, the milling speed was 250 rpm with a milling time of 6 h, the Ni and Fe nanoparticles were uniformly dispersed around W particles, and the sufficiently high sphericity of the W matrix particles was maintained. Combining the above, 3D microscopic GO-RT models with different powder morphologies were established (Figure 6).

The calculated laser absorptivity and their standard deviations are presented in Figure 7. As shown from Figure 7A, the laser absorptivity of the 90W-Ni-Fe powder bed model tended to decrease with the increase of milling energy. The laser absorptivity decreased significantly when the matrix particles were broken or deformed. The standard deviation of calculated laser absorptivity tended to decrease and then increased with the milling energy increasing (Figure 7B). The standard deviation was lowest when the reinforced particles were uniformly distributed and the matrix particles were unbroken or undeformed, indicating that the laser energy conversion factor was high and stable. This was attributed to the improved homogeneity of the powder bed^[25,26,29]. When the nanoparticles were agglomerated, the decreased ratio of spot size to irradiated particles promoted the multiple reflections of the laser, improving the laser absorptivity^[8]. However, the powder bed was uneven in this case, so the laser energy conversion was instability, which tended to produce highly unstable molten pools, affecting the printing quality of LPBF^[8,14,22]. When the matrix particles were broken or deformed, the powder bed had low packing density and high porosity, which weakened the multiple reflections and reduced the laser energy conversion factor, affecting the wetting and spreading of melt during LPBF^[8,30,31]. These may cause balling effects and reduce the printing quality of fabricated specimens^[8,24,31].

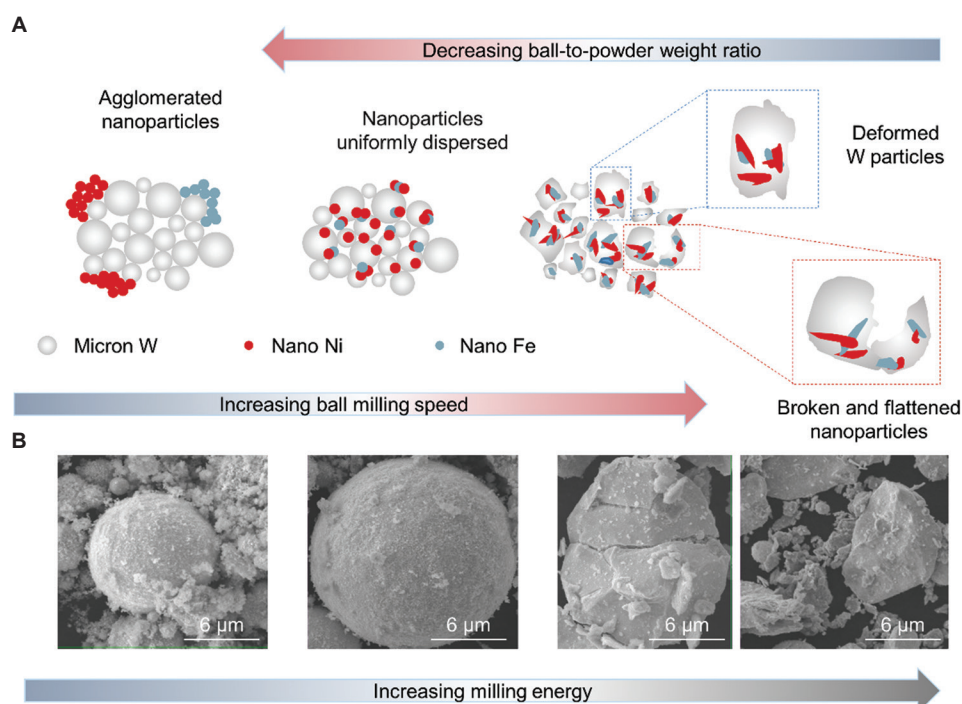


Figure 5. Schematic of the evolution mechanism of nanoparticle-coated powder during ball milling (A) and SEM images showing the different nanoparticle-coated 90W-Ni-Fe powder (B).

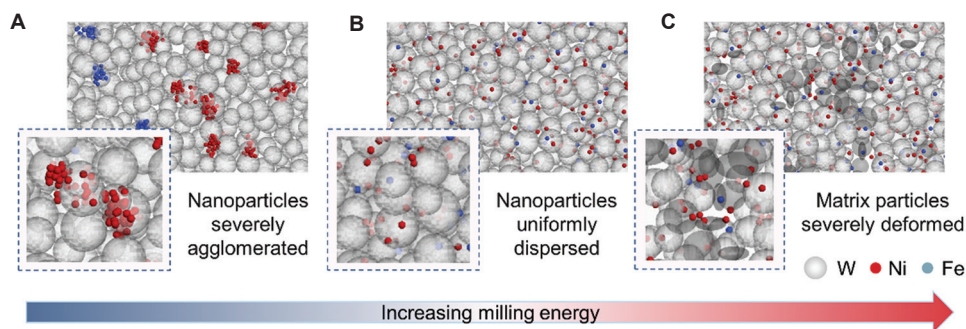


Figure 6. GO-RT models displaying different powder morphologies: severely agglomeration (A), uniformly dispersion (B), and deformation (C).

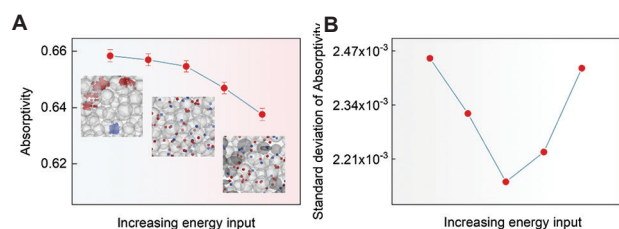


Figure 7. Calculated laser absorptivity of different models (A) and standard deviation of the absorptivity (B).

Moreover, the interaction and penetration of laser beams also have an important influence on the quality of LPBF printing^[13,22,25]. To further investigate the effect of powder morphologies on the laser absorption behavior of LPBF, analysis surfaces were established in both horizontal and vertical directions (Figure 8A), which were used to compare spot tracking results and irradiance distribution of different powder bed models. The track spot diagram on the upper surface and the irradiance in the depth direction of the powder bed were shown in Figure 8B, and it can be seen that tracking spots appeared outside the laser spot range due to the optical effect of external diffusion, which promoted heat conduction and thermal radiation^[14]. When the nanoparticles were uniformly dispersed and the sphericity of matrix particles was good, the irradiance in the depth direction was the highest and the laser interaction on the upper surface was the strongest. However, when the nanoparticles were agglomerated or the matrix particles were broken or deformed, the laser penetration was lower, and the laser interaction on the surface of the powder bed was weaker. Moreover, the laser beam tracking spot was significantly reduced when agglomerated nanoparticles adhered to matrix particles, which can be regarded as a certain masking effect^[14]. When the nanoparticles were agglomerated, the laser absorptivity of the powder bed was the highest, but most of the energy acted on nanoparticles, which weakened the interaction between matrix particles and laser, reducing the laser energy acting on matrix particles^[25,26].

The above shows that homogeneous nanoparticle-coated 90W-Ni-Fe powder with high sphericity has the best laser absorption behavior. Agglomerated nanoparticles make beams reflecting between nanoparticles and reduce the stability of absorption, and deformed particles weaken the multiple reflections and reduce the laser absorptivity and penetration.

To verify the above simulation results, the laser absorptivity/reflection of nanoparticle-coated powders with different morphologies were tested (Figure 9). Two sets of nanoparticle-coated 90W-Ni-Fe powders with different morphologies were prepared at different milling speeds or ball-to-powder weight ratios. The energy in ball milling increased with the increase of ball-to-powder weight ratio or milling speed as shown in equation VII^[28]. As seen in Figure 9, the laser absorptivity of different nanoparticle-coated 90W-Ni-Fe powders decreased with the increase of milling energy. Moreover, it decreased significantly when the milling energy was too high (matrix particle deformed). The trend of experimental results was consistent with simulation, indicating that the homogeneous nanoparticle-coated powder with high sphericity has sound laser absorption behavior with laser absorptivity of 93.51%. Similar to what has been reported, the values of measured laser absorptivity have a certain increment compared with simulation^[16]. This can be attributed to the balance between complexity and reality when constructing the model, the nanoparticles in the model are less than the actual, so the ratio of spot size to the number of irradiated particles is increased, reducing the laser absorptivity^[8,22]. At the same time, the actual W powder has a higher surface roughness than particles in the model, which also increases the measured laser absorptivity^[8,14,16,22]. Although the calculated laser absorptivity of models is lower, the models still reflect the laser absorption behavior during LPBF. Moreover, these models can visualize some phenomena which are often challenging to observe in real-time in a mesoscopic view, providing a relatively in-depth physical analysis of laser

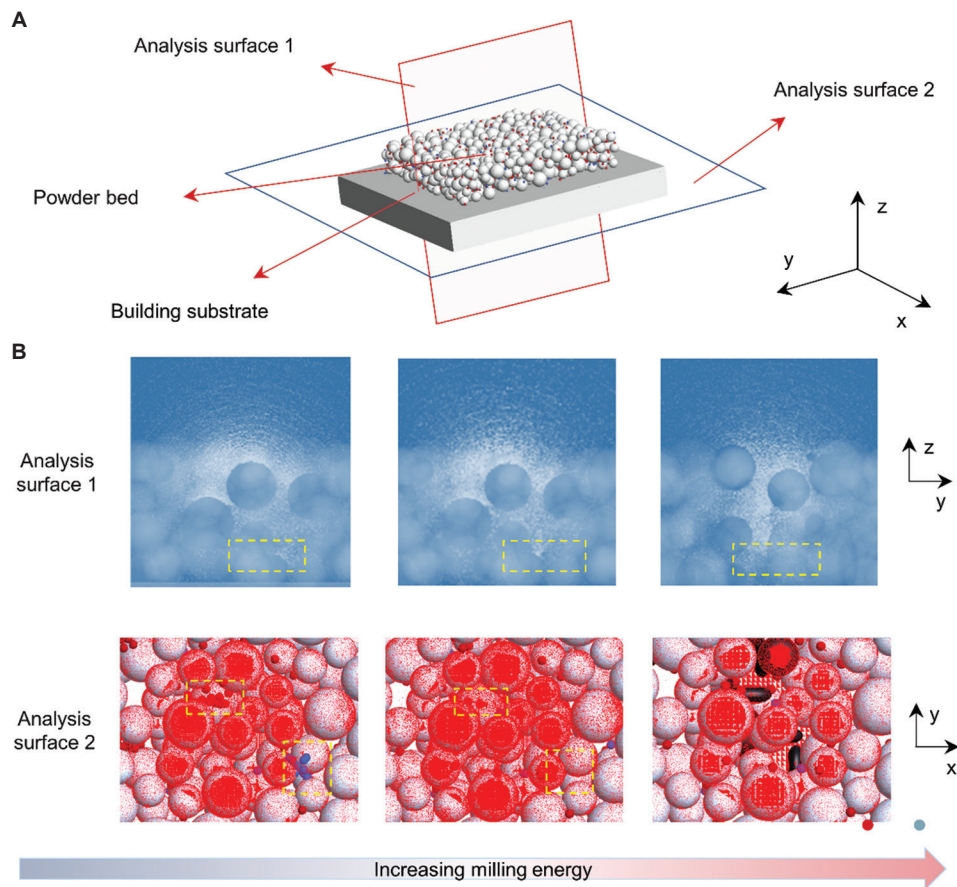


Figure 8. The analysis surfaces creating the energy irradiance in powder beds (A), and the track spot diagram of each laser ray on the surface of powder beds (B).

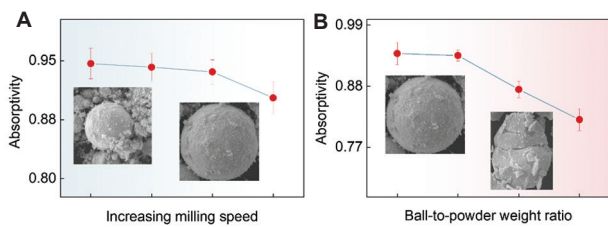


Figure 9. Absorptivity of milled nanoparticle-coated 90W-Ni-Fe powder at different milling speeds (A) and ball-to-powder weight ratios (B).

absorption behavior during LPBF fabricating W-based alloys.

3.2. Effects of nanoparticle-coated 90W-Ni-Fe powder morphologies on printability

During LPBF fabricating, the powder particles undergo complex laser-material interactions^[13]. The laser absorptivity/reflection, the number of laser interactions, and the irradiation depth predict the efficiency of the laser energy utilization of the powder bed^[14,22]. The laser utilization efficiency influences the molten pool

formation, evaporation, Marangoni effect, and recoil pressure, which determine the printing quality of LPBF-processed components^[8,14,22,24,25]. Hence, the change in laser absorption behavior due to the nanoparticle-coated 90W-Ni-Fe powder morphology is of great importance. To further reveal the influence of nanoparticle-coated 90W-Ni-Fe powder morphology on the printability, the CFD-PM single track simulation clouds (Figure 10A-C) and SEM images of LPBF-fabricated 90W-Ni-Fe scanning tracks (Figure 10D-F) were obtained. The W particles reached their melting point when the Ni and Fe particles had already reached their boiling points. Due to such a huge difference between W and Ni-Fe phases, only the W matrix particles were shown in the CFD-PM simulation clouds, the effect of enhanced particles was reflected by changing laser energy conversion factors. The melting behavior and surface quality of LPBF-fabricated single track of 90W-Ni-Fe were sensitive to the morphology of powder feed as presented in Figure 10. The LPBF scanning track was relatively straight when the reinforcing particles were uniformly distributed and the matrix particles

maintained good sphericity (Figure 10B and E), which can be attributed to the high and relatively stable laser absorption of the powder layer^[24-26]. The fully melted particles and stable molten pool improved the wetting and spreading of liquid metal, enhancing the surface quality of the LPBF-processed parts^[14,25]. Comparatively, with enhanced particles agglomerated (Figure 10A and D), the LPBF 90W-Ni-Fe single track had a fluctuated boundary. This can be attributed to the high and uneven laser absorption behavior which caused the nonuniform spreading^[11,24,26]. When the matrix particles were broken or deformed, the LPBF scanning track morphology changed to irregular shapes (Figure 10F), and the balling effects were observed (Figure 10C), which can be attributed to the increase in viscosity. When the temperature of the laser-irradiated zone is higher than the melting point of W, the viscosity of the W droplet can be defined as^[30]:

$$\eta_d(T) = 0.108 \exp\left(\frac{1.28 \times 10^5}{RT}\right) \quad (8)$$

where η_d is the viscosity of the W droplet, R is the gas constant (equal to $8.31 \text{ J}\cdot\text{mol}^{-1}\cdot\text{K}^{-1}$), and the temperature T ranges of $3350\text{--}3700 \text{ K}$. From the above equation, the higher the molten pool temperature, the lower the W droplet viscosity. The previous studies indicated that there is a competing mechanism for the wetting, spreading, and solidification of W droplets during LPBF^[31]. Due to the low laser absorptivity of the powder layer with deformed matrix particles, the molten pool cannot absorb enough

laser energy, reducing the temperature of the droplet. This increased the viscosity of the droplet and they solidified before spreading sufficiently, resulting in the balling effects. This phenomenon is detrimental to interlayer bonding and tends to affect the densification behavior during LPBF^[31,32].

Before LPBF fabrication, a computer-aided design model of the part is processed by software to plan the laser path line-by-line^[4,33]. Therefore, the quality of the scanning track is of great importance to metallurgical bonding and the surface quality of fabricated components^[6,14,24]. To further investigate the effect of nanoparticle-coated 90W-Ni-Fe powder morphology on LPBF printing quality, SEM images of the upper surfaces, and morphology of the side surfaces of different fabricated 90W-Ni-Fe alloys are presented in Figure 11. It can be seen that the evolution of the powder morphology does affect the surface quality of LPBF-processed specimens due to the changes in dynamic viscosity. LPBF processing involves the flow and solidification of liquid metal in the molten pool; the dynamic viscosity η_f of the molten pool is defined as^[29]:

$$\eta_f = \frac{16}{15} \sqrt{\frac{m}{kT}} \sigma \quad (9)$$

where m is the atomic mass, k is the Boltzmann constant, T is the temperature of the molten pool, and σ is the surface tension. The previous studies indicated that the surface tension is higher when the molten pool temperature is lower^[21]. Therefore, the higher the molten pool temperature, the lower the dynamic viscosity. The laser

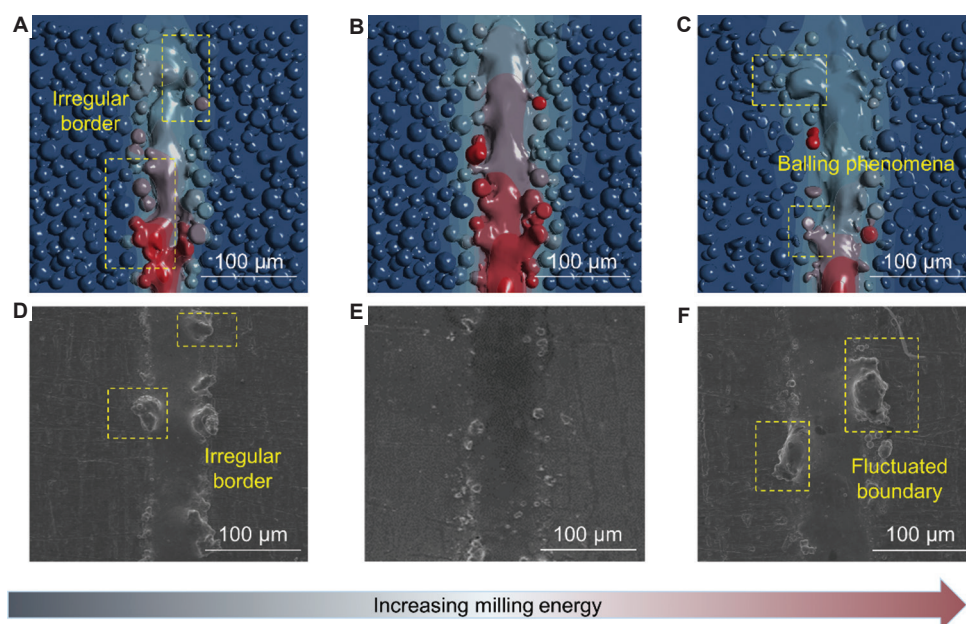


Figure 10. Simulated single-track morphologies (A-C) and SEM images showing as-fabricated 90W-Ni-Fe scanning tracks (D-F) with powders of different morphologies: severely agglomeration (A and D), uniform dispersion (B and E), and deformation (C and F).

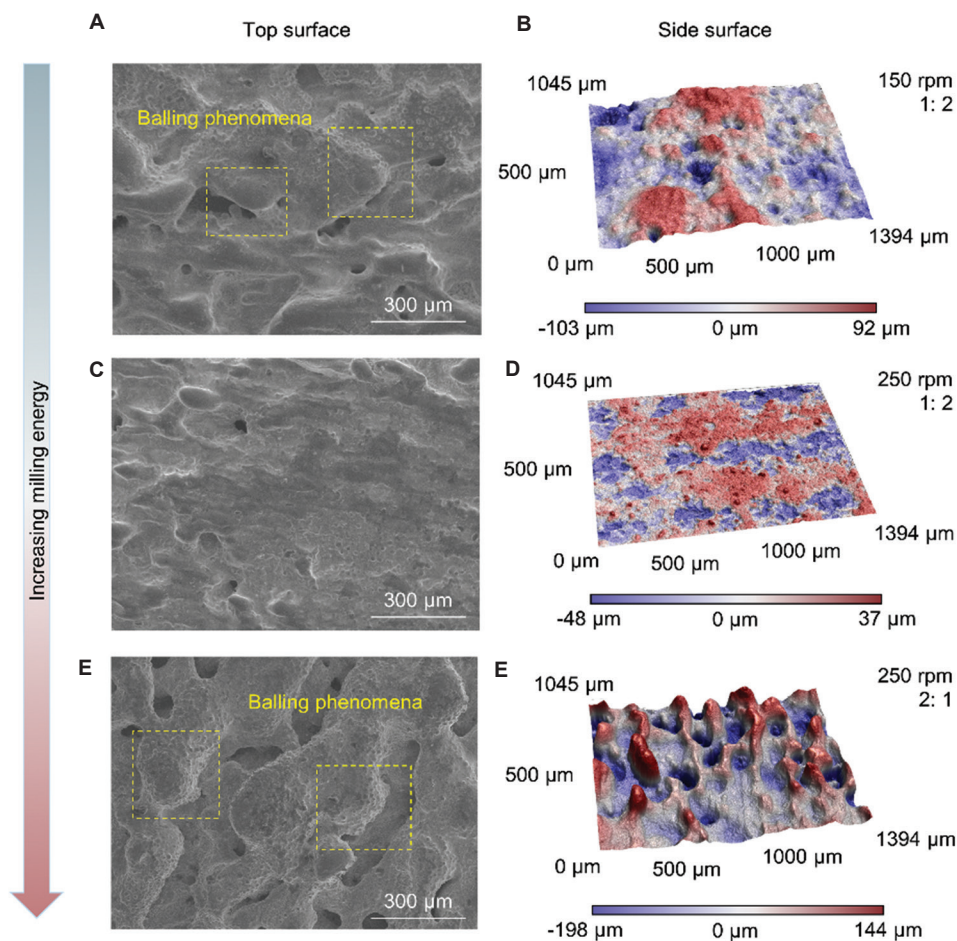


Figure 11. SEM images showing top surface morphologies (A, C, and E) and 3D morphologies describing the side surface (B, D, and F) of LPBF-processed 90W-Ni-Fe alloys fabricated by different powder: severely agglomeration (A and B), uniformly dispersion (C and D), and deformation (E and F).

energy conversion factor of the homogeneous powder with good sphericity was high and stable, lowering the dynamic viscosity of the molten pool, and yielding a sufficient liquid lifetime for wetting and spreading behavior^[14,24]. Hence, the spattering and balling effects were reduced, improving the surface quality of LPBF-fabricated 90W-Ni-Fe parts. In this instance, the surface roughness (S_a) of the fabricated specimen was 7.91 μm . When the enhanced particles were agglomerated or the matrix particles were deformed, the surface roughness (S_a) of the fabricated specimen was 20.05 μm and 29.41 μm , respectively. This can be attributed to the unstable laser absorption behavior which reduced the stability of the molten pool, leading to the splashing and balling effects, reducing the surface quality of the LPBF-processed specimens^[14,24-26].

The stability of the molten pool also tends to affect the densification behavior of LPBF-fabricated 90W-Ni-Fe alloys, which has an important influence on its mechanical properties^[4,13,34]. To investigate the effects of powder

morphologies on the densification level of LPBF-processed 90W-Ni-Fe parts, OM images of specimens fabricated by different powders were observed (Figure 12). The densification level of the specimens increased and then decreased as the milling energy increased. Homogeneous powder with high sphericity had the highest densification level (density of 98%). This was attributed to the fact that homogeneous nanoparticle-coated 90W-Ni-Fe powder with high sphericity had the best laser absorption behavior, thus improving the wetting and spreading behavior of LPBF^[29,30]. The trends of results obtained from the single tracks and bulk fabrications were correlated. With the high quality of the scanning track, the metallurgical bonding of processed specimens improved, thereby increasing the density of the fabricated W-Ni-Fe specimen.

The above results show that the powder morphology does influence the LPBF printing quality of 90W-Ni-Fe alloys and homogeneous powder with high sphericity has the sound laser absorption behavior; these help

with obtaining the best LPBF printability. Meanwhile, a good agreement is obtained between the simulated and experimental results.

3.3. Mechanical properties of the optimal 90W-Ni-Fe alloys

The above analysis shows that optimal specimens can be obtained by homogeneous nanoparticle-coated 90W-Ni-Fe powder with high sphericity. The density of LPBF-fabricated specimens has an important influence on their microhardness and residual stress distribution^[25,35]. Figure 13 presented the microhardness and residual stress distribution of the optimal specimen. The average Vickers hardness and residual stress of the 90W-Ni-Fe specimen were 439.47 HV₁ and 501.85 MPa, respectively. The dispersion of hardness values was smaller than reported, which was attributed to the high densification level of the specimen^[2]. When the load was applied to the surface of the specimen, there was no obvious collapse due to its high densification level^[36]. It is shown from Figure 13B that compressive stress was uniformly distributed inside the specimen. This can be attributed to the rapid melting-solidification process during LPBF, which produced solidification shrinkage, and the shrinkage can be expressed as^[37]:

$$\frac{d(\Delta L / L_0)}{d_t} = \frac{\Delta P_f \varepsilon_d}{D_G \eta} \quad (10)$$

where ΔP is the capillary pressure, D_G is the grain radius, ε_d is the liquid thickness, and η is the viscosity of the liquid. The optimized 90W-Ni-Fe powder formed a homogeneous powder bed, making the solidification shrinkage rate at different positions similar. Hence, the residual stress was uniformly distributed in the specimen and the gradient of residual stress was small.

The residual stress generated by the heating-cooling thermal cycle of the LPBF processing is one of the key factors affecting the properties of fabricated parts. It has been reported that LPBF-processed specimens with smaller residual stress gradients are less prone to deformation, so they have better mechanical properties^[35,37]. The compressive stress-strain curve of the testing part fabricated by optimized powder was presented in Figure 14. The compressive strength of the 90W-Ni-Fe part was 1255.35 MPa with an elongation of 24.74%, which was higher than the reported LPBF-fabricated W specimen (compressive strength of 902 MPa with an elongation of 6.4%)^[38]. To reveal the strengthening mechanisms, the microstructures of LPBF-processed W and W-Ni-Fe along the building direction were shown in Figure 15. The microstructures of LPBF-processed W consisted of large columnar grains. With the addition of nano Ni and Fe, the microstructures of the fabricated specimen presented the equiaxial columnar grains, and the cracks were significantly reduced. The

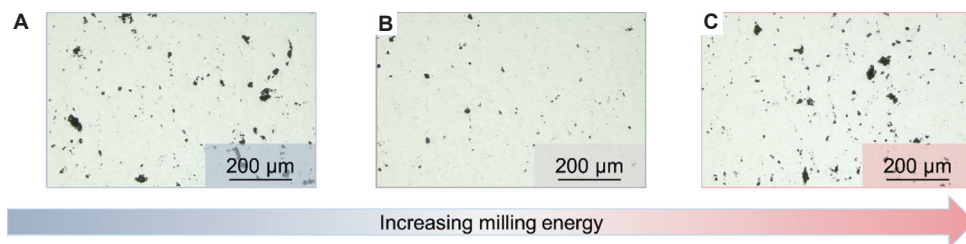


Figure 12. OM images showing LPBF-processed alloys fabricated by different nanoparticle-coated 90W-Ni-Fe powder: severely agglomeration (A), uniformly dispersion (B), and deformation (C).

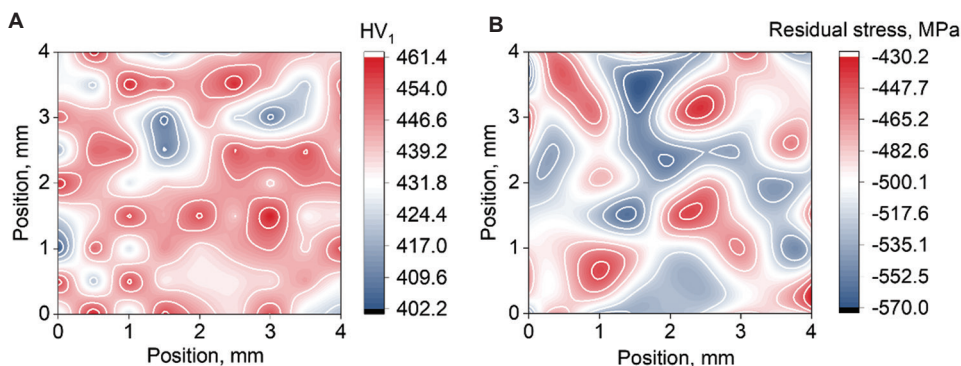


Figure 13. Hardness (A) and residual stress (B) distribution of LPBF-processed sample fabricated by optimized nanoparticle-coated 90W-Ni-Fe powder.

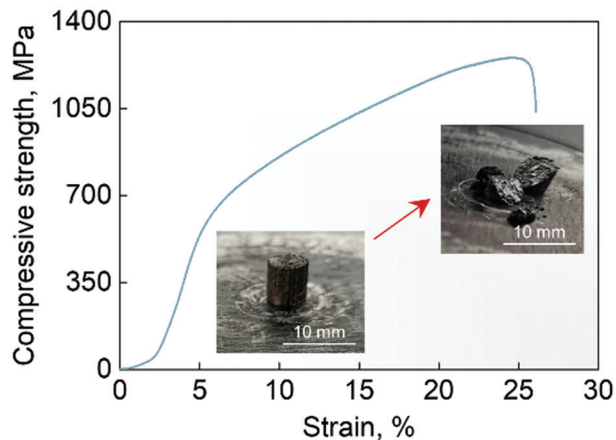


Figure 14. Compressive stress-strain curve of LPBF-processed part fabricated by optimized nanoparticle-coated 90W-Ni-Fe powder.

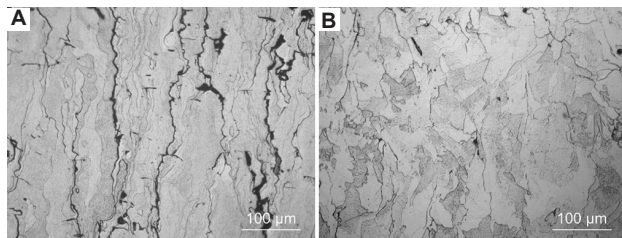


Figure 15. Microstructures of LPBF-processed W (A) and W-Ni-Fe (B) specimens.

improvement of compressive strength was attributed to the transformation of the microstructure from columnar to equiaxed grains when the Ni and Fe nanoparticles were added to the W matrix. As the surfaces of W particles were coated with Ni and Fe, the continuous growth of W grains was prevented and the growth of the equiaxed grains was promoted instead. Meanwhile, the nanoparticles were diffused to the grain boundaries due to their strong activity, reducing the microcracks and resultant grain boundary strengthening. The microstructures directly determined the mechanical properties of the final parts, thereby improving the mechanical properties of LPBF-fabricated W-Ni-Fe alloys.

4. Conclusion

Through numerical and experimental investigations, this study examined the effects of nanoparticle-coated 90W-Ni-Fe powder morphology on the laser absorption behavior and the printing quality of LPBF. GO-RT models and CFD-PM models were first established to obtain an in-depth understanding of mechanisms during LPBF fabrication of W-based alloys. Nanoparticle-coated 90W-Ni-Fe powders were prepared and corresponding alloys were fabricated by a self-developed device. Based on

the above discussion and results, several conclusions can be drawn:

- (i) It was discovered that the morphology of nanoparticle-coated 90W-Ni-Fe powder prepared by different milling conditions was different; this was attributed to the difference in milling energy caused by different milling parameters. Reinforced particles were gradually dispersed uniformly with increased specific impact energy in ball milling, but particle deformation and breakage were more likely to occur.
- (ii) Powder morphology was optimized to obtain stable laser absorption behavior with high absorptivity in both horizontal and vertical directions of the powder bed. Homogeneous nanoparticle-coated 90W-Ni-Fe powder with good sphericity had the best laser absorption behavior. Agglomerated nanoparticles made laser beams reflect between nanoparticles and reduced the stability of laser absorption behavior. Deformed matrix particles weakened the multiple reflections and lowered laser absorptivity and penetration.
- (iii) Laser absorption of nanoparticle-coated 90W-Ni-Fe powder with different morphologies was different, thus making their LPBF printability different. Homogeneous nanoparticle-coated 90W-Ni-Fe powder with good sphericity had the best LPBF printability with a straight scanning track free of balling effects, which had a good agreement with modeling results.
- (iv) The 90W-Ni-Fe alloys fabricated by optimized powder had the best surface quality (surface roughness of $7.91 \mu\text{m}$), the highest densification level (density of 98%), and uniform residual stress distribution. Moreover, the 90W-Ni-Fe alloys had a uniform hardness distribution with an average value of 439.47 HV_1 , and they had better compression properties (compressive strength of 1255.35 MPa with an elongation of 24.74%) compared with LPBF-processed pure W parts.

Acknowledgments

None.

Funding

This work was supported by the Science Challenge Project (No. TZ2018006-0301-02 and No. TZ2018006-0303-03), National Natural Science Foundation of China for Creative Research Groups (Grant No. 51921003), The 15th Batch of “Six Talents Peaks” Innovative Talents Team Program (No. TD-GDZB-001), The Fundamental Research Funds for the Central Universities (NO. NC2020004), and Basic Strengthening Program (No. 2019-JCJQ-JJ-331).

Conflict of interest

Jingjia Sun, Meng Guo, Keyu Shi, and Dongdong Gu declare that they have no (potential) conflicts or competing interests with any institutes, organizations, or agencies that might influence the integrity of results or objective interpretation of their submitted works.

Author contributions

Conceptualization: Dongdong Gu

Data curation: Jingjia Sun, Meng Guo

Formal analysis: Dongdong Gu, Jingjia Sun, Meng Guo

Funding acquisition: Dongdong Gu

Investigation: Dongdong Gu, Jingjia Sun, Meng Guo

Methodology: Jingjia Sun, Meng Guo, Keyu Shi

Project administration: Dongdong Gu, Meng Guo

Resources: Dongdong Gu

Software: Jingjia Sun, Keyu Shi, Meng Guo

Supervision: Dongdong Gu, Meng Guo

Validation: Dongdong Gu, Jingjia Sun, Meng Guo

Visualization: Dongdong Gu, Jingjia Sun, Meng Guo, Keyu Shi

Writing – original draft: Jingjia Sun

Writing – review and editing: Dongdong Gu, Meng Guo.

References

- Ivekovic A, Montero-Sistiaga ML, Vanmeensel K, *et al.*, 2019, Effect of processing parameters on microstructure and properties of tungsten heavy alloys fabricated by SLM. *Int J Refract Met Hard Mater*, 82: 23–30.
<http://doi.org/10.1016/j.ijrmhm.2019.03.020>
- Li JF, Wei ZY, Zhou BK, *et al.*, 2019, Densification, microstructure and properties of 90W-7Ni-3Fe fabricated by selective laser melting. *Metals Basel*, 9: 884.
<http://doi.org/10.3390/met9080884>
- Thompson MK, Moroni G, Vaneker T, *et al.*, 2016, Design for additive manufacturing: Trends, opportunities, considerations, and constraints. *Cirp Ann-Manuf Techn*, 65: 737–760.
<http://doi.org/10.1016/j.cirp.2016.05.004>
- Gu DD, Shi XY, Poprawe R, *et al.*, 2021, Material-structure-performance integrated laser-metal additive manufacturing. *Science*, 372: eabg1487.
<http://doi.org/10.1126/science.abg1487>
- Bourell DL, Rosen DW, Leu MC, 2014, The roadmap for additive manufacturing and its impact. *3D Print Addit Manuf*, 1: 6–9.
<http://doi.org/10.1089/3dp.2013.0002>
- Schmidt M, Merklein M, Bourell D, *et al.*, 2017, Laser based additive manufacturing in industry and academia. *Cirp Ann-Manuf Techn*, 66: 561–583.
<http://doi.org/10.1016/j.cirp.2017.05.011>
- Field AC, Carter LN, Adkins NJ, *et al.*, 2020, The effect of powder characteristics on build quality of high-purity tungsten produced via laser powder bed fusion (LPBF). *Metall Mater Trans A*, 51: 1367–1378.
<http://doi.org/10.1007/s11661-019-05601-6>
- Zhang JY, Gu DD, Yang Y, *et al.*, 2019, Influence of particle size on laser absorption and scanning track formation mechanisms of pure tungsten powder during selective laser melting. *Engineering*, 5: 736–745.
<http://doi.org/10.1016/j.eng.2019.07.003>
- Braun J, Kaserer L, Stajkovic J, *et al.*, 2019, Molybdenum and tungsten manufactured by selective laser melting: Analysis of defect structure and solidification mechanisms. *Int. J Refract Met Hard Mater*, 84: 104999.
<http://doi.org/10.1016/j.ijrmhm.2019.104999>
- AlMangour B, Grzesiak D, Yang JM, 2017, Selective laser melting of TiB₂/316L stainless steel composites: The roles of powder preparation and hot isostatic pressing post-treatment. *Powder Technol*, 309: 37–48.
<http://doi.org/10.1016/j.powtec.2016.12.073>
- AlMangour B, Grzesiak D, Yang JM, 2018, *In situ* formation of TiC-particle-reinforced stainless steel matrix nanocomposites during ball milling: Feedstock powder preparation for selective laser melting at various energy densities. *Powder Technol*, 326: 467–478.
<http://doi.org/10.1016/j.powtec.2017.11.064>
- Hu ZP, Zhao YN, Guan K, *et al.*, 2020, Pure tungsten and oxide dispersion strengthened tungsten manufactured by selective laser melting: Microstructure and cracking mechanism. *Addit Manuf*, 36: 101579.
<http://doi.org/10.1016/j.addma.2020.101579>
- Khairallah SA, Martin AA, Lee JR, *et al.*, 2020, Controlling interdependent meso-nanosecond dynamics and defect generation in metal 3D printing. *Science*, 368: 660–665.
<http://doi.org/10.1126/science.aay7830>
- Ge Q, Gu DD, Dai DH, *et al.*, 2021, Mechanisms of laser energy absorption and melting behavior during selective laser melting of titanium-matrix composite: role of ceramic addition. *J Phys D Appl Phys*, 54: 115103.
<http://doi.org/10.1088/1361-6463/abcdce>
- Ren ZH, Zhang DZ, Fu G, *et al.*, 2021, High-fidelity modelling of selective laser melting copper alloy: Laser reflection behavior and thermal-fluid dynamics. *Mater Design*, 207: 109857.
<http://doi.org/10.1016/j.matdes.2021.109857>
- Boley CD, Mitchell SC, Rubenchik AM, *et al.*, 2016, Metal powder absorptivity: Modeling and experiment. *Appl Opt*, 55: 6496–6500.

- <http://doi.org/10.1364/ao.55.006496>
17. Mosallanejad MH, Niroumand B, Aversa A, *et al.*, 2021, *In-situ* alloying in laser-based additive manufacturing processes: A critical review. *J Alloys Compd*, 872: 159567.
<http://doi.org/10.1016/j.jallcom.2021.159567>
 18. Huang S, Narayan RL, Tan JH, *et al.*, 2021, Resolving the porosity-unmelted inclusion dilemma during *in-situ* alloying of Ti34Nb via laser powder bed fusion. *Acta Mater*, 204: 116522.
<http://doi.org/10.1016/j.actamat.2020.116522>
 19. Zhang XH, Xiao Z, Yu WH, *et al.*, 2022, Influence of erbium addition on the defects of selective laser-melted 7075 aluminium alloy. *Virtual Phys Prototyping*, 17: 406–418.
<http://doi.org/10.1080/17452759.2021.1990358>
 20. Sing SL, Huang S, Goh GD, *et al.*, 2021, Emerging metallic systems for additive manufacturing: *In-situ* alloying and multi-metal processing in laser powder bed fusion. *Prog Mater Sci*, 119: 100795.
<http://doi.org/10.1016/j.pmatsci.2021.100795>
 21. Guo M, Gu DD, Xi LX, *et al.*, 2019, Selective laser melting additive manufacturing of pure tungsten: Role of volumetric energy density on densification, microstructure and mechanical properties. *Int J Refract Met Hard Mater*, 84: 105025.
<http://doi.org/10.1016/j.ijrmhm.2019.105025>
 22. Yang Y, Gu DD, Dai DH, *et al.*, 2018, Laser energy absorption behavior of powder particles using ray tracing method during selective laser melting additive manufacturing of aluminum alloy. *Mater Design*, 143: 12–19.
<http://doi.org/10.1016/j.matdes.2018.01.043>
 23. Xia MJ, Gu DD, Yu GQ, *et al.*, 2016, Selective laser melting 3D printing of Ni-based superalloy: Understanding thermodynamic mechanisms. *Sci Bull*, 61: 1013–1022.
<http://doi.org/10.1007/s11434-016-1098-7>
 24. Dai DH, Gu DD, Ge Q, *et al.*, 2020, Mesoscopic study of thermal behavior, fluid dynamics and surface morphology during selective laser melting of Ti-based composites. *Comput Mater Sci*, 177: 109598.
<http://doi.org/10.1016/j.commatsci.2020.109598>
 25. Lin KJ, Fang YM, Gu DD, *et al.*, 2021, Selective laser melting of graphene reinforced titanium matrix composites: Powder preparation and its formability. *Adv Powder Technol*, 32: 1426–1437.
<http://doi.org/10.1016/j.apt.2021.03.003>
 26. Zhuang J, Gu DD, Xi LX, *et al.*, 2020, Preparation method and underlying mechanism of MWCNTs/Ti6Al4V nanocomposite powder for selective laser melting additive manufacturing. *Powder Technol*, 368: 59–69.
<http://doi.org/10.1016/j.powtec.2020.04.041>
 27. Attar H, Prashanth KG, Zhang LC, *et al.*, 2015, Effect of powder particle shape on the properties of In Situ Ti-TiB composite materials produced by selective laser melting. *J Mater Sci Technol*, 31: 1001–1005.
<http://doi.org/10.1016/j.jmst.2015.08.007>
 28. Mio H, Kano J, Saito F, *et al.*, 2004, Optimum revolution and rotational directions and their speeds in planetary ball milling. *Int J Miner Process*, 74: S85–S92.
<http://doi.org/10.1016/j.minpro.2004.07.002>
 29. Gu DD, Shen YF, 2009, Effects of processing parameters on consolidation and microstructure of W-Cu components by DMLS. *J Alloys Compd*, 473: 107–115.
<http://doi.org/10.1016/j.jallcom.2008.05.065>
 30. Paradis PF, Ishikawa T, Yoda S, 2005, Viscosity of liquid undercooled tungsten. *J Appl Phys*, 97: 106101.
<http://doi.org/10.1063/1.1896432>
 31. Zhou X, Liu XH, Zhang DD, *et al.*, 2015, Balling phenomena in selective laser melted tungsten. *J Mater Process Technol*, 222: 33–42.
<http://doi.org/10.1016/j.jmatprotec.2015.02.032>
 32. Zhang DQ, Cai QZ, Liu JH, *et al.*, 2011, Research on process and microstructure formation of W-Ni-Fe alloy fabricated by selective laser melting. *J Mater Eng Perform*, 20: 1049–1054.
<http://doi.org/10.1007/s11665-010-9720-3>
 33. DebRoy T, Wei HL, Zuback JS, *et al.*, 2018, Additive manufacturing of metallic components process, structure and properties. *Prog Mater Sci*, 92: 112–224.
<http://doi.org/10.1016/j.pmatsci.2017.10.001>
 34. Martin JH, Yahata BD, Hundley JM, *et al.*, 2017, 3D printing of high-strength aluminium alloys. *Nature*, 549: 365–369.
<http://doi.org/10.1038/nature23894>
 35. Li C, Liu ZY, Fang XY, *et al.*, 2018, Residual stress in metal additive manufacturing. *Procedia CIRP*, 71: 348–353.
<http://doi.org/10.1016/j.procir.2018.05.039>
 36. Abbas MA, Yan AR, Wang ZY, 2021, On the use of EBSD and microhardness to study the microstructure properties of tungsten samples prepared by selective laser melting. *Materials*, 14: 1215.
<http://doi.org/10.3390/ma14051215>
 37. Zhu HH, Lu L, Fuh JY, 2004, Influence of binder's liquid volume fraction on direct laser sintering of metallic powder. *Mat Sci Eng A-Struct*, 371: 170–177.
<http://doi.org/10.1016/j.msea.2003.11.048>
 38. Gu DD, Guo M, Zhang HM, *et al.*, 2020, Effects of laser scanning strategies on selective laser melting of pure tungsten. *Int J Extrem Manuf*, 2: 025001.
<http://doi.org/10.1088/2631-7990/ab7b00>